Combustion and Flame 282 (2025) 114513

Contents lists available at ScienceDirect

Combustion and Flame

journal homepage: www.sciencedirect.com/journal/combustion-and-flame

Soot formation in iso-octane counterflow diffusion flames

Petros Vlavakis [1], Fabian P. Hagen [1,*], Alexandra Loukou, Dimosthenis Trimis

Karlsruhe Institute of Technology (KIT), Engler-Bunte-Institute, Combustion Technology, Karlsruhe, Germany

ARTICLE INFO

Keywords:
Counterflow diffusion flames
Soot formation
Iso-octane
Soot precursors
PAHs

ABSTRACT

This study investigates soot formation in laminar iso-octane counterflow diffusion flames (CDFs) under varying strain rates and fuel mass fractions. Spatially resolved measurements of temperature, major and minor gas-phase species, including polycyclic aromatic hydrocarbons (PAHs) up to three fused aromatic rings, as well as properties of the formed soot particles, such as volume fractions, primary particle sizes, and optical properties, i.e., refractive-index function for absorption in the near-infrared spectral region $E(m,\lambda_{NIR})$, were conducted using both intrusive and non-intrusive diagnostics. With increasing fuel mass fraction, the concentrations of C_1 to C_3 hydrocarbons and soot precursor molecules increase. This in turn results in higher soot volume fractions and larger particle sizes in the investigated CDFs of iso-octane. The evolution of the nanostructure and maturity of soot particles can be tracked via $E(m,\lambda_{NIR})$, which increases with rising fuel mass fractions and indicates extended basic structural units and a decreasing carbon-to-hydrogen ratio. Similarly, increasing strain rate reduces PAH concentrations, thereby affecting soot volume fractions, particle sizes, and maturity due to shortened residence times. The unique dataset aims to better understand the effects of alkane branching on soot formation by systematically investigating laminar iso-octane CDFs, and to elucidate the transition from precursor molecules to primary soot particles, including their molecular fine structure. In addition, the dataset is intended to contribute to the validation and development of kinetic mechanisms and soot models.

1. Introduction

Soot nanoparticles, in the atmospheric context referred to as black carbon, are known to influence both climate and human health. While earlier studies suggested that black carbon ranks among the most significant contributors to anthropogenic radiative forcing [1], more recent assessments indicate a lower, yet non-negligible, impact compared to greenhouse gases [2,3]. Independently of its climate relevance, the inhalation of soot particles poses a severe health risk due to their ability to penetrate deep into the respiratory system [4,5]. Consequently, regulations targeting soot emissions, particularly in the transportation sector, have become increasingly stringent. A fundamental understanding of soot formation mechanisms is therefore critical for developing strategies to mitigate particulate emissions from combustion processes.

Soot formation remains one of the most complex and unresolved phenomena in combustion science. It involves interactions between gas-phase chemistry, particle inception and growth, aggregation dynamics, and energy transport across a wide range of spatial and temporal scales [6]. Especially challenging is the transition from small hydrocarbon intermediates to large polycyclic aromatic hydrocarbons (PAHs), incipient particles, and eventually mature soot aggregates, which is governed by both chemical kinetics and local flame condition [7,8]. The overall process is sensitive to parameters such as temperature, pressure, residence time, stoichiometry, and strain rate [9–12].

To isolate key mechanisms of soot formation, canonical flame configurations with well-defined boundary conditions are employed. Laminar counterflow diffusion flames (CDFs) are particularly suitable for fundamental studies due to their aerodynamic stabilization, minimal heat losses to burner surfaces, and the ability to systematically vary the strain rate as an experimental control parameter [11,12]. Moreover, their quasi-one-dimensional structure enables simplified numerical modeling, even for large chemical reaction networks. Increased strain rates have been shown to reduce soot formation by shortening residence times for molecular growth and particle nucleation [11,13,14], whereas higher fuel mass fractions tend to enhance soot formation by increasing precursor concentrations [14,15]. These features make CDFs an ideal platform for mechanistic soot studies and model development.

* Corresponding author.
E-mail address: fabian.hagen@kit.edu (F.P. Hagen).
[1] These authors contributed equally.

https://doi.org/10.1016/j.combustflame.2025.114513
Received 19 December 2024; Received in revised form 19 August 2025; Accepted 24 September 2025
Available online 29 September 2025

The choice of fuel plays a central role in understanding soot formation. Real-world fuels such as gasoline, diesel, and aviation fuels are composed of hundreds of hydrocarbon species, including linear and branched alkanes, cycloalkanes, and aromatics [16-20]. To reduce chemical complexity while maintaining key combustion-relevant properties, surrogate fuels consisting of a limited number of representative components are commonly employed - both to enable detailed modeling and to allow for well-controlled experiments under defined boundary conditions. Investigating individual components of such surrogate mixtures, such as iso-octane, is valuable for isolating the influence of specific molecular structures on soot formation pathways and for developing predictive kinetic models before extending to more complex multi-component systems. As a representative compound mimicking branched alkanes, iso-octane is frequently used as a surrogate component due to its relevance to gasoline, diesel, and synthetic aviation fuels [16–20]. While its combustion characteristics such as ignition delay [21, 22] and flame speed [23,24] have been widely investigated, there is a notable lack of comprehensive studies on PAH and soot formation in iso-octane diffusion flames.

Previous studies have focused on individual aspects of soot formation in iso-octane flames. Zeng et al. [25] analyzed soot precursors in premixed configurations, while Frenzel et al. [26] quantified soot particle size distributions and volume fractions in similar flame types. Liu et al. [27] investigated soot precursor chemistry in a coflow diffusion flame, yet without soot measurements. Kruse et al. [28] reported soot volume fractions in iso-octane CDFs under varying strain rates and fuel mass

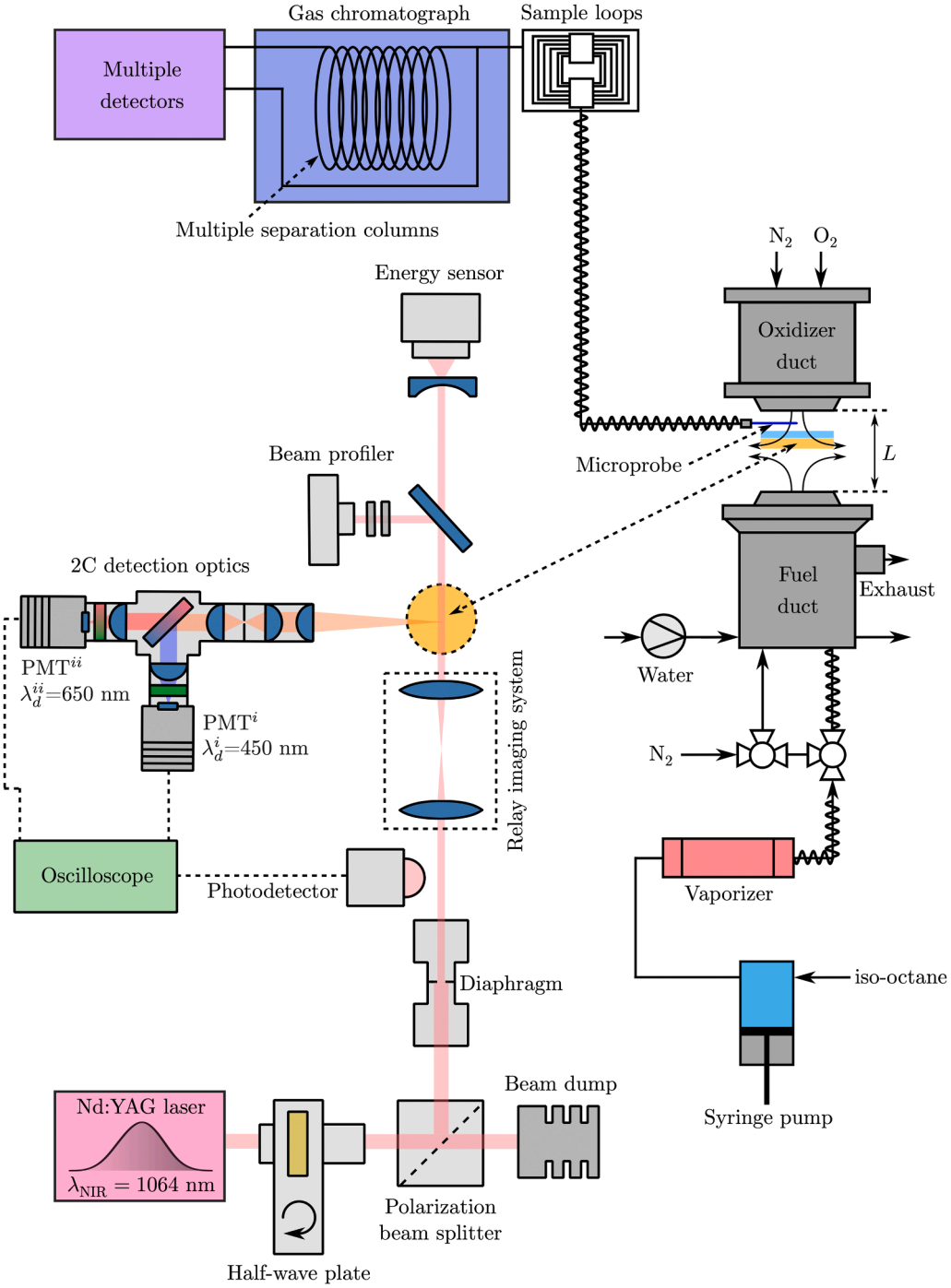

Fig 1. Experimental setup.

fractions but did not provide PAH profiles or temperature data. Conversely, Sarathy et al. [29] and Zhao et al. [30] presented PAH concentration profiles in iso-octane CDFs; however, only Sarathy et al. [29] reported temperature profiles, and neither study included soot measurements.

This study addresses the identified gap by providing spatially resolved measurements of temperature and PAH concentrations in iso-octane CDFs across a range of strain rates and fuel mass fractions. In addition, soot volume fractions, primary particle sizes, and optical properties are quantified using both intrusive and non-intrusive diagnostics. The resulting dataset enables a deeper understanding of the relationship between gas-phase chemistry and soot formation, including the molecular fine structure and carbon-to-hydrogen ratio of the resulting particles. The data may serve as a basis for the further development and validation of kinetic soot models capable of describing both molecular and optical properties of soot. This study thereby provides a controlled benchmark for extending soot modeling efforts to more complex fuel mixtures.

2. Experimental approach

In this study, we investigate CDFs of iso-octane, which are characterized by the flame stabilized on the oxidizer side of the stagnation plane (SP) and are referred to as soot formation (SF) CDFs [31]. In this configuration, the soot particles formed are convected in the opposite direction to the oxidizer flow, thus suppressing soot oxidation. The CDFs of SF type are realized at moderate oxygen mole fractions on the oxidizer side, meaning that soot formation takes place in a zone of low oxygen concentration. The overall process is dominated by particle formation and particle dynamics [11,14,31], offering the opportunity to focus on the transition from precursor molecules to primary soot particles.

The flame structure is quantified using intrusive methods. While the temperature profiles are measured using a thermocouple probe, PAHs up to pyrene are sampled using a microprobe and quantified via gas chromatography (GC) coupled to different detectors. Soot volume fractions, primary particle sizes and optical properties of particles formed in the investigated CDFs are analyzed by two-color time-resolved laser incandescence (2C-TiRe-LII).

Fig. 1 provides an overview of the counterflow burner, the fuel and oxidizer supply system and the diagnostic methods employed in this study and outlined in the following sections.

2.1. Counterflow burner and fuel supply system

The investigated CDFs were stabilized in a counterflow burner designed by Niemann, Seshadri and Williams at the University of California San Diego [32]. This water-cooled counterflow burner is moveable in vertical direction, sketched in Fig 1 and described in detail in [14,33,34], consists of two identical, opposing ducts with an internal diameter of 25 mm and a fixed separation distance L of 12.5 mm. The fuel mixture is fed through the bottom duct and the oxidizer mixture, i.e., air in this study, is fed through the top duct. Both ducts are surrounded by ring-shaped channels that enable the CDFs to be shielded with a nitrogen sheath flow. Oxidizer and sheath flow gases of highest purity are supplied via mass flow controllers (MFCs). Fine stainless steel wire meshes made of 50 μm diameter wires are mounted at the duct exits to promote approximate plug-flow conditions. The resulting velocity field has been experimentally shown to be close to plug flow, justifying the use of average velocities to estimate strain rates [32]. The exhaust gases are removed via a separate second ring-shaped duct around the fuel duct.

The liquid fuel, i.e., iso-octane, was supplied to the counterflow burner in gaseous form via a liquid fuel preparation system consisting of a syringe pump (500D, Teledyne ISCO, USA) and a direct vaporizer (aSTEAM, aDROP Feuchtemesstechnik GmbH, Germany). Depending on the fuel mass fraction, a defined volume flow of nitrogen is added to the gaseous fuel downstream of the vaporizer. The fuel lines were conditioned at 400 K to prevent condensation of the liquid components in the lines and/or in the burner. The iso-octane, i.e., 2,2,4-Trimethylpentane, CAS number: 540-84-1, used in this study has a purity of 99.99 %.

2.2. Investigated iso-octane counterflow diffusion flames

Following the nomenclature of [14,33,34], the indices 1 and 2 denote the fuel and oxidizer duct respectively. In the experiments, a momentum balance of the opposing reactant streams, $\rho_1 v_1^2 = \rho_2 v_2^2$, is imposed to keep the stagnation plane approximately in the middle between the two ducts. Here, v_1 and v_2 denote the flow velocities of the fuel and oxidizer flow normal to the stagnation plane, while ρ_1 and ρ_2 are the associated densities. The average velocities of the reactants are estimated as the ratio of the corresponding volumetric flow rates to the cross-sectional area of the ducts. In the region between the stagnation plane and the oxidizer duct, the characteristic strain rate a_2, defined as the normal gradient of the normal component of the flow velocity, evaluated in the stagnation plane, is given by [34,35]:

$$a_2 = \frac{2\,|v_2|}{L}\left(1+\frac{|v_1|\,\sqrt{\rho_1}}{|v_2|\,\sqrt{\rho_2}}\right). \quad (1)$$

Due to the momentum equilibrium, the strain rate a_2 is directly correlated with the flow rate of the oxidizer mixture and separation distance between the two ducts and can be approximated by $a_2 = 4\,|v_2|\,L^{-1}$ [14]. Here, the fuel mass fraction is denoted by $Y_{F,1}$, but is abbreviated as Y_F for simplicity, as neither partially premixed nor premixed flames are investigated in this study. The oxygen mass fraction of the oxidizer $Y_{O_2,2}$ is kept constant at 0.233 in this study.

As listed in Table 1, a total of eight iso-octane CDFs at different fuel mass fractions and strain rates were investigated. All experiments are carried out at atmospheric pressure.

As a first diagnostic step, sooting limits in CDFs were determined using elastic light scattering, following the approach by Joo et al. [36]. A continuous-wave laser emitting at 532 nm was directed through the burner axis, and the scattered light was detected by a photomultiplier tube with narrow-band and polarization filtering; the resulting signal was demodulated using a lock-in amplifier synchronized with a mechanical chopper to improve the signal-to-noise ratio. The transition from non-sooting to sooting conditions is identified by the appearance of a local maximum in the normalized scattering intensity profile, indicating the presence of soot particles [34,36].

As a baseline case, a non-sooting CDF with a strain rate of 60 s^{-1} and a fuel mass fraction of 0.35 is investigated. The experimental data obtained are used to evaluate the performance of the available chemical kinetic mechanisms. Then, the fuel mass fraction is varied from 0.35 to 0.60 at a constant strain rate of 60 s^{-1}. The strain rate is finally varied from 60 s^{-1} to 120 s^{-1} at a constant fuel mass fraction of 0.60.

2.3. Quantifying the flame structure

The flame structure is investigated by measuring the temperature

Table 1
Investigated iso-octane CDFs. The sooting limit was determined using the method proposed by Joo et al. [36].

Flame		Fuel		Oxidizer		Sooting tendency
	a_2 / s^{-1}	$Y_F = Y_{F,1}$	$Y_{N_2,1}$	$Y_{O_2,2}$	$Y_{N_2,2}$	
1	60	0.35	0.65	0.233	0.767	non-sooting flame
2	60	0.47	0.53	0.233	0.767	sooting flame
3	60	0.50	0.50	0.233	0.767	sooting flame
4	60	0.60	0.40	0.233	0.767	sooting flame
5	70	0.60	0.40	0.233	0.767	sooting flame
6	80	0.60	0.40	0.233	0.767	sooting flame
7	100	0.60	0.40	0.233	0.767	non-sooting flame
8	120	0.60	0.40	0.233	0.767	non-sooting flame

and the major and minor species along the flame axis, with the profiles determined as a function of distance from the fuel duct. The intrusive diagnostic methods for determining the flame structure are presented in the following two sub-sections.

2.3.1. Measurement of temperature profiles

The axial temperature profiles of the investigated flames were measured using an S-type thermocouple probe, as described in our previous studies [14,34,37]. A spring mechanism prevents deformation of the thin thermocouple wires with a diameter of 100 μm, which are fixed under tension parallel to the reaction zone [14]. To eliminate catalytic effects, the wires were coated with zirconium oxide, resulting in a thermocouple bead with a diameter of 400 μm. The measured temperatures were corrected for radiation losses according to [38], with further details provided in [14,34]. The influence of soot deposition on emissivity was considered negligible due to the short residence time of less than three seconds and the absence of observable soot deposits, confirmed by optical microscopy. Considering the standard deviation of the measurements and the uncertainties imposed by the radiation correction, the uncertainty of the reported temperatures is 80 K [14,34,37].

2.3.2. Measurement of gas-phase species profiles

A gas chromatograph (GC) coupled with multiple detectors was employed to quantify the spatially resolved gas-phase composition. For sampling the local gas-phase, a chemically inert ceramic microprobe with an inner and outer diameter of 300 μm and 500 μm, respectively, coupled to the GC was used, see also Fig 1. This microprobe approach was previously proposed by Carbone and Gomez [39] and adopted by us in a modified design.

For sampling, the microprobe is moved horizontally into the stabilized CDFs using a traverse system. The vertical movement in steps of 500 μm to measure the gas-phase composition along the flame axis, i.e., distance from the fuel duct (DFD), was carried out with the traversable counterflow burner, see Section 2.1. The position of the microprobe relative to the flame was monitored using a CCD camera. To ensure accurate registration of the measurement position, the visible blue and red emission layers - corresponding to CH* chemiluminescence and Planck radiation from soot particles, respectively - were used as fixed optical markers. Image analysis confirmed that the lateral displacement of the flame front caused by the probe was consistently below 200 μm and thus smaller than the vertical scan step. This intrusive method therefore causes a spatial uncertainty that is primarily related to the step size and probe positioning and is conservatively estimated as ± 500 μm.

The transfer line connecting the microprobe with the GC is heated up to 423 K to prevent condensation of gas-phase species. A total of 15 storage loops, each with a volume of 10 ml, conditioned at 503 K, enabled consecutive sampling at different DFD of the CDFs. An automated routine was used to analyze all gas samples [40].

A GC coupled with multiple detectors, which is described in detail elsewhere [33], served to determine the gas-phase composition. Three GC columns connected to a thermal conductivity detector (TCD) were used to quantify CO, CO_2, O_2, H_2 and H_2O. Another GC column separated lighter, i.e., $< C_5$, and higher hydrocarbons. Both fractions were quantified by two separate GC columns and by flame ionization detectors (FID) and mass spectrometry (MS).

The GC, including the multiple detectors, was calibrated with gaseous and liquid mixtures. Calibration of major gas-phase species was performed with reference gas mixtures consisting of CO, CO_2, O_2, H_2, N_2, CH_4, C_2H_2 and C_6H_6. Higher hydrocarbons and PAHs were calibrated with liquid reference mixtures using the syringe pump and a direct vaporizer, see Section 2.1., or by liquid injection. Both methods showed excellent agreement and were used for different concentration levels. To ensure accurate quantification, all species subjected to quantitative analysis were calibrated in a two-point calibration. The overall uncertainty on reported concentrations is ± 3-10 % for the main species and ± 5-30 % for light and heavy hydrocarbons, which include PAHs, and ± 20 % for water. These values correspond to the largest uncertainty of the species in the flames studied, considering the standard deviations of three repeated measurements and the uncertainties from the calibration procedures.

2.4. Quantifying optical properties, volume fractions and primary particle size distributions of soot particles

In this work, two-color time-resolved laser-induced incandescence (2C-TiRe-LII) is applied to quantify the optical properties, volume fractions and primary particle size distributions of the soot particles formed in iso-octane CDFs. 2C-TiRe-LII involves detecting thermal radiation emitted by a nano-sized particle ensemble that has been heated by nanosecond laser pulse absorption [41,42]. The theoretical approaches of 2C-TiRe-LII to derive the target quantities is presented in Section 2.4.1. and the optical setup in Section 2.4.2.

2.4.1. Approaches of 2C-TiRe-LII

The temperature increase of an ensemble of spherical primary particles induced by laser pulse absorption is given by the energy balance [43,44]:

$$\frac{N_P\ \pi\ \rho_P}{6}\int_0^{\infty}\int_{T_P^0}^{T_P^*} d_P^3\ c_s\ P(d_P)\ dT\ dd_P = \frac{N_P\ \pi^2\ E(m,\lambda_{exc})\ f_{exc}}{\lambda_{exc}}\int_0^{\infty} d_P^3\ P(d_P)\ dd_P. \tag{2}$$

Here, T_P is the particle temperature, with T_P^0 and T_P^* indicating the temperatures before and after laser pulse absorption, respectively. Further, ρ_P, d_P, N_P and c_s refer to the density, size, number and volumetric heat capacity of the laser-heated particles. The size distribution function of the particle ensemble within the detection volume is given by $P(d_P)$. According to [45,46], $P(d_P)$ can be approximated best by a log-normal distribution function:

$$P(d_P) = \left[\sqrt{2\pi}\ d_P \ln(\sigma_g)\right]^{-1} \exp\left[-\frac{[\ln(d_P) - \ln(CMD)]^2}{2[\ln(\sigma_g)]^2}\right]. \tag{3}$$

Here, the count median diameter *CMD* and the geometric standard deviation σ_g represent the first and second moment of the distribution function. In this study, a twofold approach regarding σ_g is applied. Comparable to [14], a constant geometric standard deviation of $\sigma_g = 1.4 = const.$ is used to ensure the best comparability of count median diameters. In addition, a variable σ_g is used as a function of the DFD. The evolving σ_g values were derived from mobility sizing, applied to track the soot formation process, and originate from CDFs of comparable strain rates and fuel mass fractions in [47], albeit for ethylene flames.

In Eq. (2), λ_{exc} is the wavelength of the excitation laser pulse and f_{exc} is its laser fluence integrated over the pulse duration. Further, $E(m,\lambda_{exc})$ is the refractive-index function for absorption of the absorbing particle ensemble at the excitation wavelength [48]. Since an excitation wavelength in the near infrared (NIR) spectral range was used, i.e., $\lambda_{exc} = \lambda_{NIR} = 1064$ nm, we can specify $E(m,\lambda_{exc}) = E(m,\lambda_{NIR})$.

According to [44,49,50], $E(m,\lambda_{NIR})$ depends on the molecular structure of the soot particles. On a molecular scale, nano-sized soot particles are composed of graphene-like basic structural units (BSUs) with statistically distributed size [44]. As the size of the BSUs increases, the optical band gap decreases, increasing the probability of absorption of low-energy photons. Consequently, the light absorption of the particles in the NIR increases, resulting in an increase in the values of $E(m,\lambda_{NIR})$. Based on this, the evolution of the molecular structure and/or the maturity [51–53] of soot particles during their formation can be monitored by measuring $E(m,\lambda_{NIR})$.

By applying Eq. (2) and assuming a temperature-independent volumetric heat capacity, i.e., $\rho_P\ c_s$, [45,54], $E(m,\lambda_{NIR})$ can be determined by

measuring the particle temperature before and after absorption of a laser pulse with known fluence [49,52,55,56]:

$$E(m,\lambda_{NIR}) \cong \frac{\lambda_{NIR}\,\rho_P\,c_s}{6\pi\,f_{exc}}\left[T_P^* - T_P^0\right]. \tag{4}$$

The initial particle temperature T_P^0 is assumed equal to the local gas temperature, as soot particles are in thermal equilibrium with the surrounding gas prior to laser heating. This gas temperature is obtained from the gas-phase measurements described in Section 2.3.1. The post-laser temperature, T_P^*, was determined via 2C pyrometry, as outlined in the following section. $E(m,\lambda_{NIR})$ can thus be calculated for the investigated soot particles in the absorption-dominated regime [56], i.e., in the low fluence regime. This approach is subject to several sources of uncertainty, as discussed in detail in Section 3.

Applying Planck's radiation law, the temperature of the laser-heated soot particle ensemble is derived. For homogeneous and optically thin conditions inside the laser probe volume [45], the thermal radiation signal $S(\lambda_d,\ T_P)$ at a discrete detection wavelength λ_d follows Planck's radiation law integrated over all solid angles [45,49,57]:

$$S(\lambda_d,\ T_P) = N_P \int_0^\infty \frac{8\,\pi^3 h\,c_\lambda^2\,E(m,\lambda_d)\,\Sigma_d\,d_P^3\,P(d_P)}{\lambda_d^6}\left[\exp\left[\frac{h\,c_\lambda}{\lambda_d\,k_B\,T_P}\right]-1\right]^{-1} dd_P. \tag{5}$$

The spectral response of the signal detection system is accounted via Σ_d. Further, k_B is Boltzmann's constant, h Planck's constant and c_λ the speed of light. Assuming Wien's approximation, i.e., $\exp(h\,c_\lambda/\lambda_d\,k_B\,T_P) \gg 1$ [58], the temperature of the laser-heated soot particle ensemble can be calculated from the ratio of the thermal radiation signals, $S(\lambda_d^i,\ T_P)$ and $S(\lambda_d^{ii},\ T_P)$, see Eq. (5), at two different detection wavelengths, λ_d^i and λ_d^{ii}, respectively [41,42,45,49,57–59]:

$$T_P = \frac{h\,c_\lambda}{k_B}\left(\frac{1}{\lambda_d^{ii}}-\frac{1}{\lambda_d^{i}}\right)\left[\ln\left(\frac{S(\lambda_d^i,\ T_P)\ E(m,\lambda_d^{ii})\ (\lambda_d^i)^6}{S(\lambda_d^{ii},\ T_P)\ E(m,\lambda_d^i)\ (\lambda_d^{ii})^6}\right) C_{cal}^i\right]^{-1}. \tag{6}$$

The calibration constant C_{cal}^i, which accounts for the spectral sensitivity of the detection system at the two wavelengths, is determined using a tungsten lamp [41,44,49]. In literature, e.g., [41,44,49,59], $E(m,\lambda_d^{ii})/E(m,\lambda_d^i) = 1$ is often used for detection wavelengths being not too far apart. This assumption leads to a maximum uncertainty of the particle temperatures and thus $E(m,\lambda_{NIR})$, see Eq. (4), of approx. 10 % [44,49], which is also valid for small, nascent particles in flame environments, e.g., those presented in [53]. Based on Eq. (6), T_P^*, i.e., the particle temperature directly after the laser pulse absorption can be determined, which is required to evaluate $E(m,\lambda_{NIR})$ according to Eq. (4).

Following laser pulse absorption and the accompanying prompt temperature rise, the gas-borne particle ensemble cools down to the temperature of the surrounding gas-phase. When operating 2C-TiRe-LII in the low-fluence regime, i.e., the sublimation temperature [51] is not reached during laser pulse absorption, heat conduction determines the cooling process of the particles [41,42]. Since the conductive cooling rate is proportional to particles surface area, small particles cool faster than larger ones [41]. Thus, the primary particle size distribution of the laser-heated particles can be derived from the temporal temperature decay, which in turn is determined from the measured 2C pyrometry signal, see Eq. (6).

Furthermore, the temperature decay, which depends strongly and non-linearly on the moments of $P(d_P)$, can be simulated numerically using an energy balance equation for the laser-heated particles. Assuming a log-normal distribution function, the statistical moments of the actual primary particle size distribution of the investigated soot aerosol are obtained by a multidimensional nonlinear fit of the calculated temperature decays - as a function of the particle size distribution - to those measured by 2C pyrometry [54]. In the present work, this fit is applied to the temporal decay of the TiRe-LII signal at a single detection wavelength, λ_d^i or λ_d^{ii}, which is less affected by measurement noise than the derived temperature decay and thus yields more robust results, comparable to the evaluation strategy in e.g., [59,60]. The choice of detection wavelength is not critical, as we verified that comparable results are obtained for different wavelengths. Exemplary signal decay traces and corresponding fits, obtained at different DFD in an investigated iso-octane CDF, are provided in the Supplementary Material.

In the applied simulations, particle cooling is modeled using the Karlsruhe model [44,49,61], which was first proposed by Lehre et al. [62], modified in [61], and extended by temperature-dependent expressions for c_s [59], ρ_P [63] and the sublimation enthalpy [64]. In this framework, energy losses due to heat conduction, radiation, and evaporation are considered, with evaporation being negligible in the low-fluence regime applied here. Comparable to Kock et al. [59], energy fluxes resulting from particle annealing or oxidation are neglected. The uncertainties in determining $P(d_P)$ are discussed in the context of the obtained results.

The laser pulse absorption of a particle ensemble in the Rayleigh regime is proportional to its volume within the detection volume, as shown in Eq. (2). According to Kirchhoff's law, the thermal radiation of laser-heated particles is likewise proportional to their volume. When all particles are heated to the same peak temperature - ensured by operating in the plateau fluence regime [41,42] - the peak 2C-TiRe-LII signal is approximately proportional to the soot volume fraction f_v [55]. In our original approach, which forms the basis for f_v data presented in this work, f_v was determined in the plateau regime and calibrated against a reference flame of known f_v, yielding the calibration constant $C_{cal}^j(\lambda_d^{ii})$ from:

$$f_v \cong C_{cal}^j(\lambda_d^{ii})\ S(\lambda_d,\ T_P^*). \tag{7}$$

According to [14], the uncertainty of the prompt approach can be up to 40 % when considering repeated experiments and variations in $E(m,\lambda_{NIR})$. For $f_v > 500$ ppb and $E(m,\lambda_{NIR}) > 0.3$, the measurement uncertainty decreases to below 20 %. The calibration constant $C_{cal}^j(\lambda_d^{ii})$ was determined by comparing the measured $S(\lambda_d,\ T_P^*)$ values from our laser-optical setup, see Section 2.4.2., with those obtained in a laminar, premixed ethylene/air reference flame at an equivalence ratio of 2.1, for which the soot volume fraction is known from the measurements of Hadef et al. [65].

In the extended analysis, the low-fluence data originally recorded for determining $P(d_P)$ and $E(m,\lambda_{NIR})$ were also used to derive f_v. This enabled a recursive determination of f_v using the auto-compensating approach [66], based on the particle temperature after laser pulse absorption, T_P^*, without reference flame calibration. The required $E(m,\lambda_d^{ii})$ was estimated from $E(m,\lambda_{NIR})$ determined in this study, using $E(m,$ 532 $nm)/E(m,\lambda_{NIR})$ ratios reported for comparable ethylene CDFs in [14]. These ratios, obtained following the approach of Therssen et al. [67], range from 1.1 to 1.7 depending on strain rate, fuel mass fraction, and DFD. From this range, an average Ångström coefficient of 0.45 ± 0.30 can be derived, corresponding to a conversion factor for $E(m,\lambda_d^{ii})$ relative to $E(m,\lambda_{NIR})$ between 1.08 and 1.45. The resulting uncertainty in $E(m,\lambda_d^{ii})$ directly propagates into the f_v values obtained with the auto-compensating approach, adding an estimated ± 15 % relative uncertainty on top of other measurement errors. The resulting f_v values derived via the auto-compensating approach agreed within ± 15 % of the values obtained using the reference flame calibration approach for f_v up to 500 ppb. For cases with $f_v > 500$ ppb and $E(m,\lambda_{NIR}) > 0.3$, the deviation remained below 30 %, consistent with the previously stated measurement uncertainties and confirming the robustness of our soot volume fraction data.

2.4.2. Laser-optical setup

In this study, the fundamental wavelength of a 10 Hz-pulsed Q-switched Nd:YAG laser at $\lambda_{exc} = 1064$ nm was employed. A rotating half-

wave plate and a polarizing beam splitter was used to ensure a constant and defined laser fluence. A fluence of 0.1 J cm^{-2} in the low-fluence regime was used to determine $E(m,\lambda_{NIR})$ and $P(d_P)$, as well as to derive f_v via the auto-compensating approach. In the plateau regime, a fluence of 0.4 J cm^{-2} was applied to quantify f_v using the reference flame calibration approach. Operation in the plateau regime was verified by a fluence curve study, as shown in the Supplementary Material for the critical flame in this context, characterized by $E(m,\lambda_{NIR})$ values ranging from 0.10 to 0.19 at a strain rate of 60 s^{-1} and a fuel mass fraction of 0.50. However, at a DFD of 6.5 mm and $E(m,\lambda_{NIR}) = 0.10$, operation is close to the low-fluence threshold of the plateau regime. Pulse-to-pulse fluence was measured with a calibrated fast photodiode, see [49,50], whereas the integral laser energy was measured with an energy sensor. The laser beam passes through a mirror array, an aperture [49,50] and is relay imaged to the detection volume with a 1:1 magnification. Beam monitoring was carried out with and without CDFs to prove a negligible influence of the flames on the beam profile. The 2C-TiRe-LII signal decays were collected at an angle of 120° to the laser beam with a 2C detection optics comprising a lens system and two fast photomultipliers (H10720-20, Hamamatsu Photonics, 0.5 ns rise time) with 10 nm FWHM bandpass interference filters centered at $\lambda_d^i = 450$ nm and $\lambda_d^{ii} = 650$ nm, respectively. The signal recording was carried out with a digital oscilloscope (Rohde & Schwarz RTM3004 with RTM-B2410 and RTM-B6) providing a bandwidth of 1 GHz and a sampling rate of 5 GSa/s. The triggering of the 2C detection optics was realized with the photodiode used for pulse-to-pulse fluence measurements. Details of the instruments used are provided elsewhere [14,49,50]. In data analysis, six hundred TiRe-LII signals were averaged to calculate $E(m,\lambda_{NIR})$, $P(d_P)$ and f_v.

3. Results and discussion

Section 3.1 addresses the flame structure, i.e., temperature and species concentration profiles, of a non-sooting iso-octane CDF, see Flame 1 in Table 1. This provides a reference for evaluating soot-related trends without cross-influences from surface chemistry. Section 3.2 discusses the effect of varying fuel mass fractions up to 0.60 at a constant strain rate of 60 s^{-1} on flame structure and soot formation metrics, i.e., f_v, $E(m,\lambda_{NIR})$ and $P(d_P)$. Section 3.3 presents results for varying strain rates at a constant fuel mass fraction of 0.60. For clarity, error bars are omitted in the following figures; the corresponding uncertainties of the diagnostics are detailed in Section 2 and in the data discussion.

3.1. Flame structure analysis of a non-sooting iso-octane CDF

In first experiments, the sooting limit was determined using elastic light scattering following the approach of Joo et al. [36], as described in Section 2.2. It was found to occur at a fuel mass fraction of 0.45 for a strain rate of 60 s^{-1}. Accordingly, a fuel mass fraction of 0.35 at the same strain rate was selected as the non-sooting reference CDF. This section presents the temperature profile and the concentration profiles of quantifiable species in this CDF, i.e., Flame 1 in Table 1, as a function of DFD. These profiles provide a quantitative baseline for subsequent comparison with sooting flames and for assessing the role of fuel mass fraction in soot precursor formation.

Fig. 2 presents the radiation-corrected temperature profile as a function of the DFD. The peak temperature of approximately 1720 K occurs at a DFD of 6.5 mm, followed by a gradual decline toward the oxidizer side. The temperature rise on the fuel side marks the reaction zone of the strained diffusion flame. The profile is largely symmetric with respect to the position of maximum temperature, while the stagnation plane is located further toward the fuel side at a DFD of about 5.7 mm, in agreement with previous measurements in comparable CDFs [14,29,68].

The measured volume concentration profiles of major reactants and products are shown in Fig 3. Fuel, i.e., C_8H_{18}, and oxygen are consumed

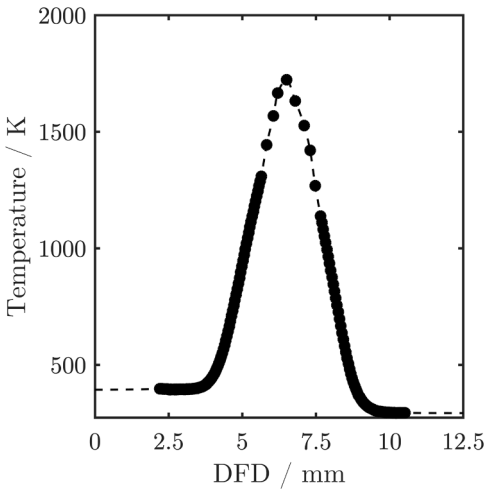

Fig 2. Radiation-corrected temperature profile of an iso-octane CDF at a strain rate of 60 s^{-1} and a fuel mass fraction of 0.35 as a function of DFD.

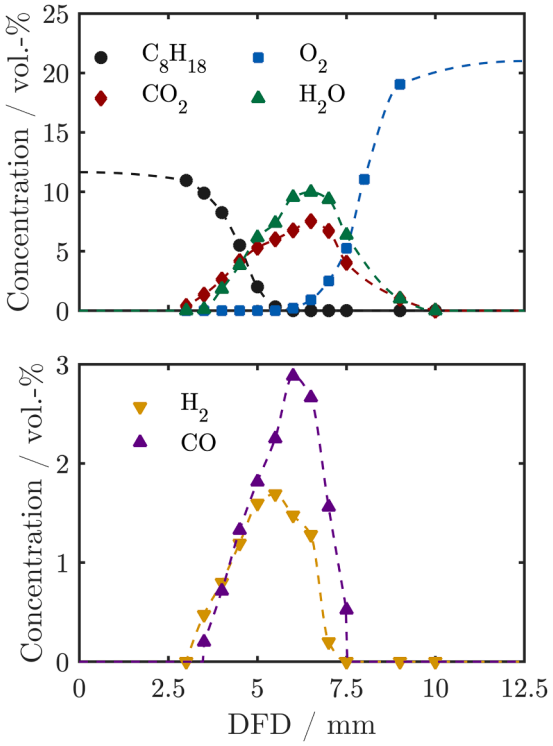

Fig 3. Concentration profiles of C_8H_{18}, O_2, CO_2, H_2O (top) and CO as well as H_2 (bottom) of an iso-octane CDF at a strain rate of 60 s^{-1} and a fuel mass fraction of 0.35 as a function of DFD.

within the narrow reaction zone between DFD of 5 mm and 6 mm. The main products, CO_2 and H_2O, peak in this region, with the H_2O maximum slightly shifted toward the oxidizer side. Hydrogen and carbon monoxide, formed as intermediate products, exhibit peaks in the same zone, with CO reaching higher concentrations than H_2.

Fig. 4 shows the measured volume concentration profiles of C_1 to C_3 hydrocarbons. Methane, CH_4, and acetylene, C_2H_2, peak near a DFD of 6 mm on the oxidizer side of the reaction zone, with C_2H_2 showing the narrowest, sharpest maximum. Ethylene, C_2H_4, and propene, C_3H_6, peak closer to a DFD of 5 mm on the fuel side with peak levels comparable to CH_4 and C_2H_2, while ethane, C_2H_6, remains lower. Propane, C_3H_8, remains at very low levels and is scaled by a factor of ten for clarity. These

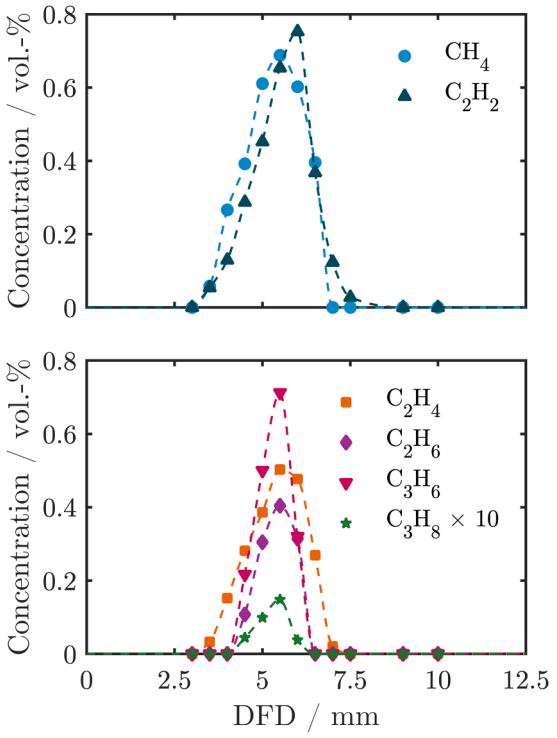

Fig 4. Concentration profiles of C_1 to C_3 hydrocarbons of an iso-octane CDF at a strain rate of 60 s^{-1} and a fuel mass fraction of 0.35 as a function of DFD. Note that the C_3H_8 concentration is shown multiplied by a factor of ten for clarity.

distributions reflect formation by thermal and oxidative decomposition of iso-octane in the reaction zone, followed by rapid consumption toward the oxidizer duct. The profiles agree well with previous studies on CDF of ethylene at comparable strain rates [14,68], confirming the reliability of the measurements.

Fig. 5 shows the volume concentration profiles of single-ring aromatic species as well as PAHs. Benzene, C_6H_6, is the dominant single ring, A1, species and exhibits its highest volume concentrations in the fuel-rich side of the reaction zone. Toluene, C_7H_8, ethylbenzene, C_8H_{10}, and the sum of xylene isomers, C_8H_{10}, i.e., ortho-, meta- and para-xylene, follow similar spatial trends but with lower concentrations. Styrene, C_8H_8, and indene, C_9H_8, show comparable profiles and magnitudes to xylene.

The first detected PAH with two fused aromatic rings, naphthalene, $C_{10}H_8$, shows a tendency to peak slightly closer to the reaction zone than benzene and other A1-based species. This behavior is consistent with its dominant formation pathway, where growth from small aromatics proceeds rapidly via hydrogen-abstraction-C_2H_2-addition (HACA) [69]. Three-ring PAHs, represented by the combined concentration of anthracene, $C_{14}H_{10}$, and phenanthrene, $C_{14}H_{10}$, as well as fluorene, $C_{13}H_{10}$, appear in trace amounts with relatively flat profiles across the oxidizer side beyond the reaction zone. Pyrene, $C_{16}H_{10}$, and higher PAHs remain below the limit of detection (LOD) of the gas-phase diagnostics under the investigated flame conditions.

The slight spatial separation between the maxima of A1-based species and PAHs indicate a transition from primary aromatic formation to PAH growth chemistry. In CDFs, such spatial trends are generally consistent with established PAH growth mechanisms: Single-ring aromatics tend to form where C_2 and C_3 hydrocarbon radicals are present in high concentrations in the high-temperature reaction zone. The profiles and relative magnitudes of the measured aromatic and PAH species are in good agreement with previous experimental studies of laminar CDFs of (toluene-doped) ethylene at comparable strain rates [70,71], supporting the quantitative accuracy of the present dataset.

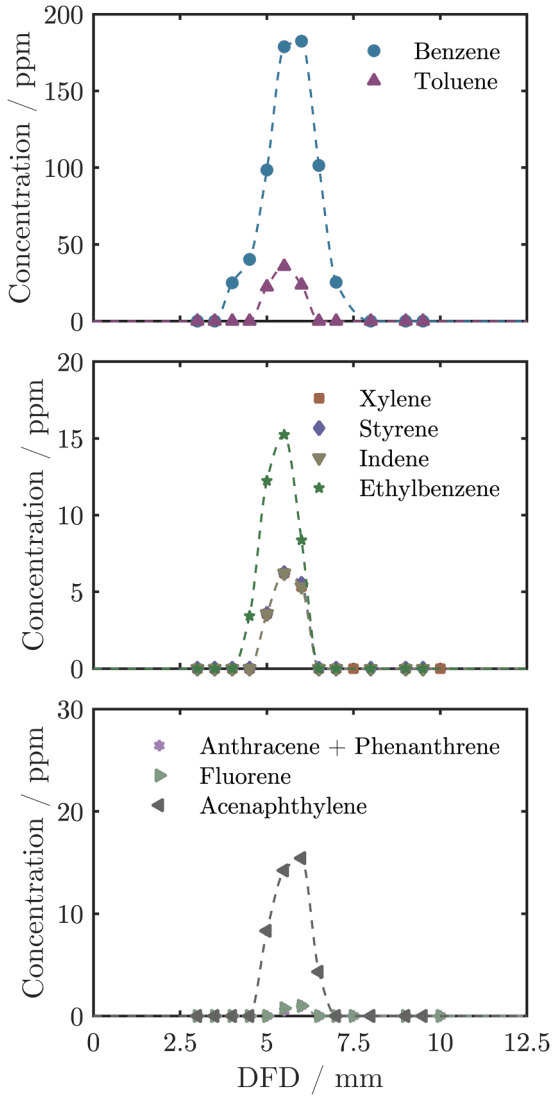

Fig 5. Concentration profiles of A1-based species and PAHs of an iso-octane CDF at a strain rate of 60 s^{-1} and a fuel mass fraction of 0.35 as a function of DFD. Note that xylene represents the isomer mixture, and the measured values are similar to those of styrene and indene. The concentrations of fluorene, as well as the total concentration of the three-ring aromatics anthracene and phenanthrene, are also similar.

3.2. *Analysis of CDFs of varying fuel mass fraction*

This section analyzes the influence of fuel mass fraction at a constant strain rate on precursor chemistry and soot formation. Temperature and species concentration profiles, as well as quantified soot properties from Flames 1 to 4, see Table 1, are presented.

With increasing fuel mass fraction, both peak temperature and width of the reaction zone increase, while the flame shifts slightly closer to the oxidizer duct. Profiles of temperature, major species, and C_1 to C_3 hydrocarbons are provided in the Supplementary Material. As expected, higher fuel mass fractions result in increased concentrations of all major species. Specifically, raising the fuel mass fraction from 0.35 to 0.60 increases CO_2 and H_2O volume concentrations from 8 % to 8.5 % and 10 % to 11.8 %, respectively. The effect is more pronounced for CO and H_2, with CO increasing from 2.8 % in Flame 1 to 4.5 % in Flame 4, while the H_2 concentration nearly doubles. A similar trend is observed for C_1 to C_3 hydrocarbons, i.e., CH_4, C_2H_4, C_2H_6, C_3H_6, C_3H_8, and C_2H_2, see Supplementary Material. Increasing the fuel mass fraction from 0.35 to 0.60 results in more than a twofold increase in the concentration of CH_4.

While C_2H_4, C_2H_6, C_3H_6, and C_3H_8 also increase, the effect is less pronounced. Fig. 6 shows that the acetylene volume concentration approximately doubles when the fuel mass fraction increases from 0.35 to 0.60, which is reflected in the benzene profile, as higher C_2H_2 levels enhance benzene formation via HACA pathways.

Fig. 7 presents concentration profiles for toluene, xylene, styrene, ethylbenzene, indene, and several higher PAHs. Fuel enrichment leads to pronounced increases in aromatic species, with some higher-ring PAHs showing particularly strong sensitivity. For example, the benzene volume concentration, shown in Fig 6, increases from 180 ppm to nearly 500 ppm, while xylene rises from about 7 ppm at $Y_F = 0.35$ to 65 ppm at $Y_F = 0.60$. Similar to acetylene, styrene, ethylbenzene, and indene concentrations show increases by factors of about two to three. Toluene also shows a clear peak increase from approx. 40 ppm to 80 ppm with higher fuel mass fraction. In addition, the onset of PAH growth is evident: naphthalene, acenaphthylene, fluorene, as well as the sum of anthracene and phenanthrene all exhibit significantly higher peak values at $Y_F = 0.60$. The PAHs exhibit concentration profiles similar to the A1-based aromatic species, with significant increases observed as the fuel mass fraction rises. Acenaphthylene shows the largest increase, from 17 ppm in Flame 1 to nearly 70 ppm in Flame 4. Naphthalene increases from 5 ppm to 20 ppm, while fluorene as well as the sum of anthracene and phenanthrene, i.e., three-ring PAHs, show a similar rise from about 1 ppm to 5 ppm. This trend is consistent with established PAH growth pathways [72], in which enhanced acetylene availability fosters ring growth. Accordingly, the larger PAHs exhibit a comparable sensitivity to fuel enrichment as the smaller aromatics.

Fig. 8 shows the soot volume fraction profiles of CDFs with varying fuel mass fractions. As described in Section 2, these CDFs are of SF type, where soot particles form on the fuel side near the flame, grow as they are convected toward the stagnation plane, SP, and eventually leak through it, resulting in a sharp decrease in soot volume fraction across the SP [12]. The profiles are similar to those reported in the literature, e.g., [11–14,28]. For Flame 2, with a fuel mass fraction of 0.47, the peak soot volume fraction approaches the LOD of 2C-TiRe-LII [47]. Increasing

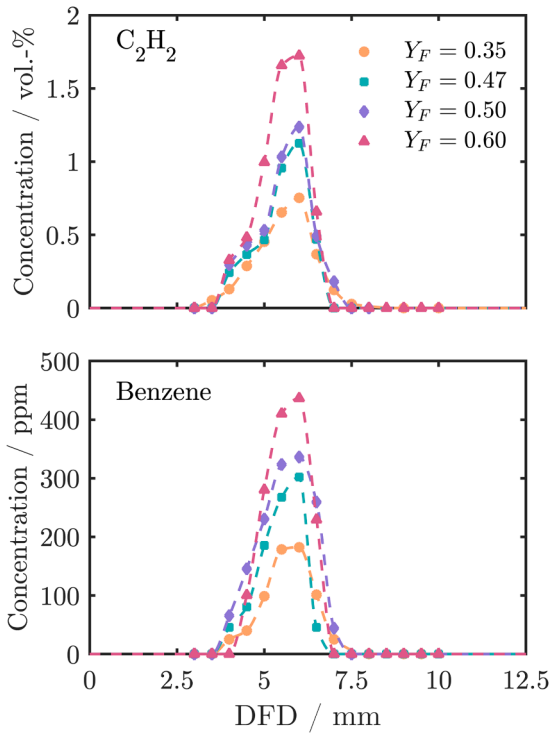

Fig 6. Symbols show the measured volume concentration profiles of acetylene and benzene obtained from iso-octane CDFs at a constant strain rate of 60 s^{-1} and varying fuel mass fractions of 0.35 to 0.60 as a function of DFD.

the fuel mass fraction to 0.50 raises the peak soot volume fraction to approx. 20 ppb. A further rise leads to a factor of 40 increase, reaching approx. 0.8 ppm. Similar trends and profiles have been reported for ethylene CDFs [15,73].

As explained in Section 2.4.1, two complementary approaches were applied to determine f_v. On the one hand, f_v was obtained in the plateau fluence regime using a reference flame, in which soot particles correspond to approximately 13 nm when approximated as monodisperse [65]. Nanostructural features, such as extended BSU sizes that likely determine $E(m, \lambda_{NIR})$ [44,49,50], correlate with primary particle size [14], with smaller primaries generally exhibiting smaller $E(m, \lambda_{NIR})$ and *vice versa* [53]. If the actual $E(m, \lambda_{NIR})$ at a specific DFD in an investigated CDF is smaller than in the reference flame, f_v can be underestimated due to the calibration, whereas larger $E(m, \lambda_{NIR})$ would cause overestimation; this effect is covered by the f_v uncertainties stated in Section 2.4.1. On the other hand, in the low-fluence regime used for the auto-compensating approach, particles of different sizes do not reach the same peak temperature due to the limited laser pulse energy, and the measured ensemble peak temperature represents an average over size-dependent values, making this method inherently more sensitive to $P(d_P)$ than operation in the plateau regime. The close agreement between f_v from the reference flame calibration and auto-compensating approaches within the stated uncertainties confirms that such effects are accounted for in the reported values.

In addition to the soot volume fraction, Fig 8 shows the quantified count median diameter of the primary particle size distribution. Starting from the oxidizer side, the primary particle size increases toward the stagnation plane, reaching its peak value near the SP, which correlates with soot volume fraction. In CDFs close to the soot limit, primary particle size is predominantly influenced by surface growth, which is driven by gas-phase chemistry and PAH concentrations. As A1-based aromatics and PAH concentrations strongly depend on the iso-octane fuel mass fraction, the increasing particle size with fuel mass fraction can be explained.

As outlined in Section 2.4.1, a twofold approach regarding the geometric standard deviation σ_g is applied. Comparable to [14], a constant value of $\sigma_g = 1.4$ was assumed to ensure the best comparability of count median diameters. In addition, a variable σ_g was considered as a function of the DFD. The evolving σ_g values were derived from mobility sizing, applied to track the soot formation process, and originate from CDFs of comparable strain rates and fuel mass fractions in [47], albeit for ethylene flames. For the variable approach, σ_g values of 1.60, 1.80, 1.80, 1.75, and 1.70 were used between 5.0 mm and 7.0 mm in 0.5 mm increments. Independent of the chosen σ_g, the fits of the time-resolved decay traces with the Karlsruhe model consistently yielded $R^2 > 0.99$, demonstrating excellent agreement. On average, the *CMD* obtained with variable σ_g decreased by about 25 % compared to the constant assumption, which is on the order of the measurement uncertainty, see paragraph below. Based on the data reported in [47], it may be assumed that the variable approach captures the broadening of the size distribution during soot growth more realistically, while the overall *CMD* trends remain robust against the chosen σ_g value.

The quantification of the count median diameter of the primary particle size distribution from 2C-TiRe-LII decays is influenced by several factors. The quality of the fit between measured decay curves and the Karlsruhe model contributes about 2 % to 5 % uncertainty. A major systematic contribution arises from the assumption for the geometric standard deviation: using either a constant value of $\sigma_g = 1.4$ or a variable σ_g obtained from mobility sizing changes the *CMD* by 5 % to 10 % and in extreme cases up to 15 %. Additional contributions result from the uncertainty of the local gas temperature with about 3 %, while effects of detector linearity are smaller than 2 %. In addition, the extrapolation of $E(m, \lambda_d^{ii})$ from $E(m, \lambda_{NIR})$ using Ångström coefficients, as described in Section 2.4.1, introduces an uncertainty of about ± 15 % in $E(m, \lambda_d^{ii})$, which propagates into the *CMD* determination and adds an

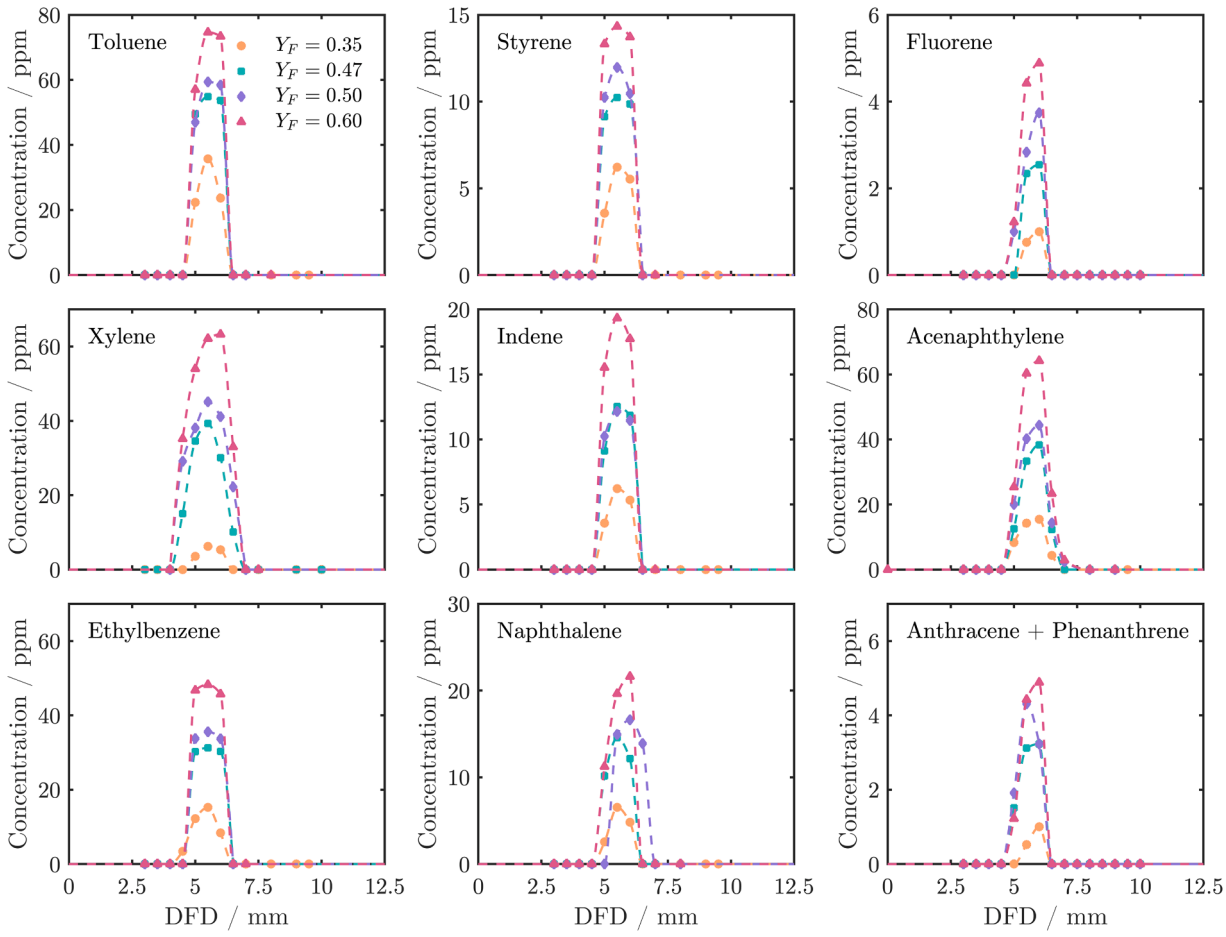

Fig 7. Symbols show the measured volume concentration profiles of A1-based aromatics and PAHs obtained from iso-octane CDFs at a constant strain rate of 60 s-1 and varying fuel mass fractions of 0.35 to 0.60 as a function of DFD. Pyrene, C16H10, and higher PAHs remain below LOD of the gas-phase diagnostics under the investigated flame conditions.

additional systematic component of roughly 10 %. These contributions were estimated using the Karlsruhe model. Altogether, these contributions yield a combined standard uncertainty of about 10 % to 15 % in *CMD*. This order of uncertainty is confirmed by comparing $P(d_P)$ with the values derived via transmission electron microscopy, see e.g., [44, 59]. To remain conservative, count median diameters are reported with an expanded uncertainty of less than 20 % with coverage factor two, explicitly including the sensitivity to the choice of σ_g and the extrapolation of $E(m, \lambda_d^{ii})$.

The refractive index function $E(m, \lambda_{NIR})$ depends on the molecular structure of the particles, which consists of BSUs with varying sizes [44, 49,51]. Large-sized BSUs reduce the optical band gap, increasing the absorption of low-energy photons, particularly in NIR spectral region. This leads to higher $E(m, \lambda_{NIR})$ values, reflecting a higher degree of graphitization and particle maturity [14,51–53,56,74]. Consequently, $E(m, \lambda_{NIR})$ can be used to monitor the structural evolution of soot during its formation. As shown in Fig 8, PAH chemistry not only influences the primary particle size and soot volume fraction but also impacts the molecular structure of soot, i.e., $E(m, \lambda_{NIR})$. Increasing fuel mass fractions result in increased concentrations of large-sized PAHs, see Fig 7. These large-sized PAHs form the framework of the developing particle during particle inception and surface growth reactions, thus shaping its carbon nanostructure. Therefore, it seems reasonable that a higher concentration of large-sized PAHs, as observed for increasing fuel mass fractions, promotes a primary particle graphitization and thereby increases $E(m, \lambda_{NIR})$. This relationship has already been demonstrated in [14], where it was also shown that $E(m, \lambda_{NIR})$ is related to the soot volume fraction.

The determination of $E(m, \lambda_{NIR})$ according to Eq. (4) involves several sources of uncertainty. As stated in Section 2.4.1, the temperature measurement of soot particles contributes about 10 %. Using the gas-phase temperature adds up to 8 %, depending on DFD. The assumed particle density introduces up to 20 % variation when comparing nascent and mature soot [75], while neglecting the temperature and maturity dependence of the volumetric heat capacity contributes on the order of 10 %. Thus, the overall uncertainty of $E(m, \lambda_{NIR})$ is estimated at up to 20 % for mature soot particles, where the density is better constrained and the higher gas-phase temperature reduces sensitivity, but may reach up to 40 % for nascent soot particles, where both density assumptions and lower reference temperatures amplify the error. Nevertheless, the relative trends of $E(m, \lambda_{NIR})$ remain robust even when accounting for these uncertainties.

3.3. Analysis of CDFs of varying strain rate

This section is divided into two distinct parts. First, the profiles of measured gas-phase species are presented and discussed for one sooting and two non-sooting flames at a constant fuel mass fraction and varying strain rates, i.e., Flames 4, 7, and 8, comparable to Section 3.2. Subsequently, the soot volume fraction, count median diameters of the primary particle size distributions and $E(m, \lambda_{NIR})$ as a function of DFD are analyzed for Flames 4, 5, and 6. For these flames, a_2 is varied from 60 s^{-1} to 80 s^{-1} at a constant fuel mass fraction.

The measured temperature profiles align with data from literature, e.g., [76], showing a decrease in both peak temperature T_{max} and width of the reaction zone as the strain rate increases from 60 s^{-1} to 120 s^{-1}. Major

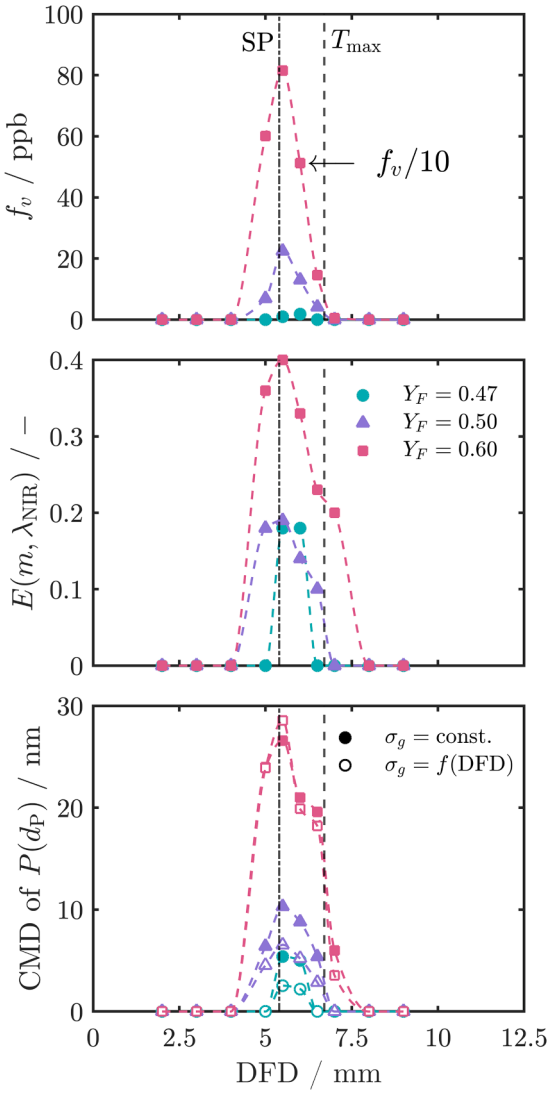

Fig 8. Soot volume fraction, refractive-index function for absorption at the laser excitation wavelength and count median diameter of the primary particle size distribution for iso-octane CDFs at a constant strain rate of 60 s^{-1} and fuel mass fractions between 0.47 and 0.60 as a function of DFD. The maximum temperature T_{max}, marking the reaction zone, and the stagnation plane, SP, are indicated. The measurement uncertainty in quantifying soot volume fractions is discussed in Section 2.4.1. Uncertainties in the analysis of the refractive-index function for absorption amount to up to 20 % for mature soot particles and up to 40 % for nascent soot in the region around 7 mm to 7.5 mm. The count median diameter is associated with a relative uncertainty of 20 %. A constant geometric standard deviation of $\sigma_g = 1.4 = const.$ is shown with open symbols, while variable σ_g values are indicated with closed symbols and amount to 1.60, 1.80, 1.80, 1.75 and 1.70 between 5.0 mm and 7.0 mm in 0.5 mm increments.

species concentration profiles reveal that the peak concentrations of CO, CO_2, H_2, and H_2O remain unaffected by the strain rate, while the widths of the profiles decrease slightly with increasing strain rate. For selected C_1 to C_3 hydrocarbons, i.e., C_3H_6 and C_2H_4, growth starts at lower DFD with increasing strain rate. Comparable to Section 3.2, profiles of temperature, major species, and C_1 to C_3 hydrocarbons are provided in the Supplementary Material.

While C_1 to C_3 hydrocarbons, in particular C_2H_6 and C_3H_6, show a systematic decrease in volume concentration with increasing strain rate, the concentration of acetylene varies unsystematically but remains within the measurement uncertainty discussed in Section 2.3.2. In contrast, benzene concentration, shown in Fig 9, is significantly affected by the strain rate, altering both profile shape and formation zone. With

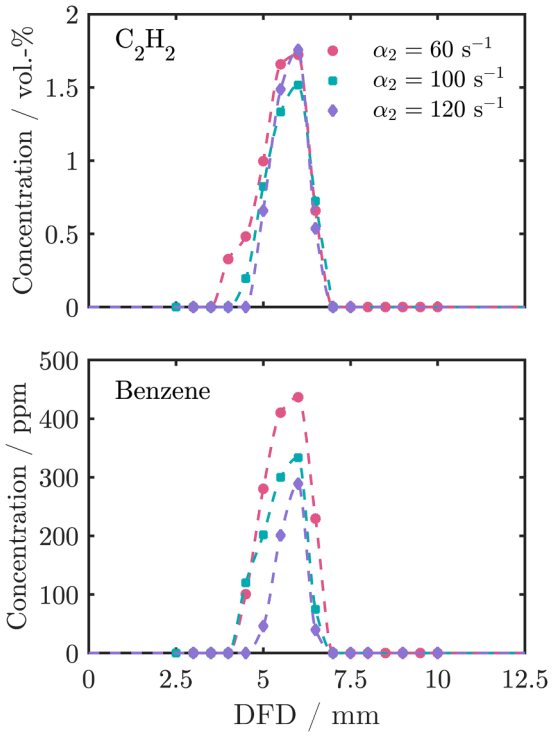

Fig 9. Symbols show the measured volume concentration profiles of acetylene and benzene obtained from iso-octane CDFs at a constant fuel mass fraction of 0.60 and varying strain rates of 60 s^{-1}, 100 s^{-1} and 120 s^{-1} as a function of DFD.

increasing strain rate, the profile becomes narrower, and the peak concentration decreases systematically.

Concentration profiles for A1-based aromatics and PAHs are shown in Fig 10. Increasing the strain rate from 60 s^{-1} to 100 s^{-1} leads to a pronounced reduction in their concentrations, with further but less distinct decreases at 120 s^{-1}. Changes in profile shape could not be resolved within the experimental uncertainty and can therefore only be inferred. At a strain rate of 60 s^{-1}, the concentrations of naphthalene and acenaphthylene are approximately twice those at 120 s^{-1}. Increasing the strain rate from 60 s^{-1} to 100 s^{-1} suppresses the formation of fluorene, anthracene and phenanthrene, which is why they are not included in Fig 10.

The observed decreases in selected C_1 to C_3 hydrocarbons, A1-based aromatics, and PAHs with increasing strain rate are attributed to the reduced residence time in the flame, which suppresses the formation of larger PAHs and consequently the formation of soot particles [12]. The latter becomes evident when comparing soot volume fraction profiles measured in sooting CDFs at different strain rates, see Fig 11. However, unlike gas-phase species, soot volume fractions were determined at different strain rates, i.e., sooting Flames 4, 5, and 6.

An increase in the strain rate from 60 s^{-1} to 70 s^{-1} reduces the peak soot volume fraction from 800 ppb to approx. 250 ppb. A further increase to 80 s^{-1} decreases the peak value by an order of magnitude. Thus, the changes in f_v are significant even when considering the uncertainties of both quantification methods, see Section 2.4.1. Further evidence is provided by the fact that these trends are consistent with literature data [11–14,47,73]. The profile shapes are similar to those observed for varying fuel mass fractions, as discussed in Section 4.2. As shown above, the decrease in PAH concentrations with increasing strain rate likely explains the reduced soot volume fractions.

As expected, particle sizes, represented by the *CMD* of $P(d_P)$, decrease with increasing strain rate due to reduced residence time, which limits surface growth and particle-particle coagulation [12]. This effect is independent of the σ_g assumption. As noted in Section 3.2, the *CMD* is on average lower when assuming variable σ_g, but remains within

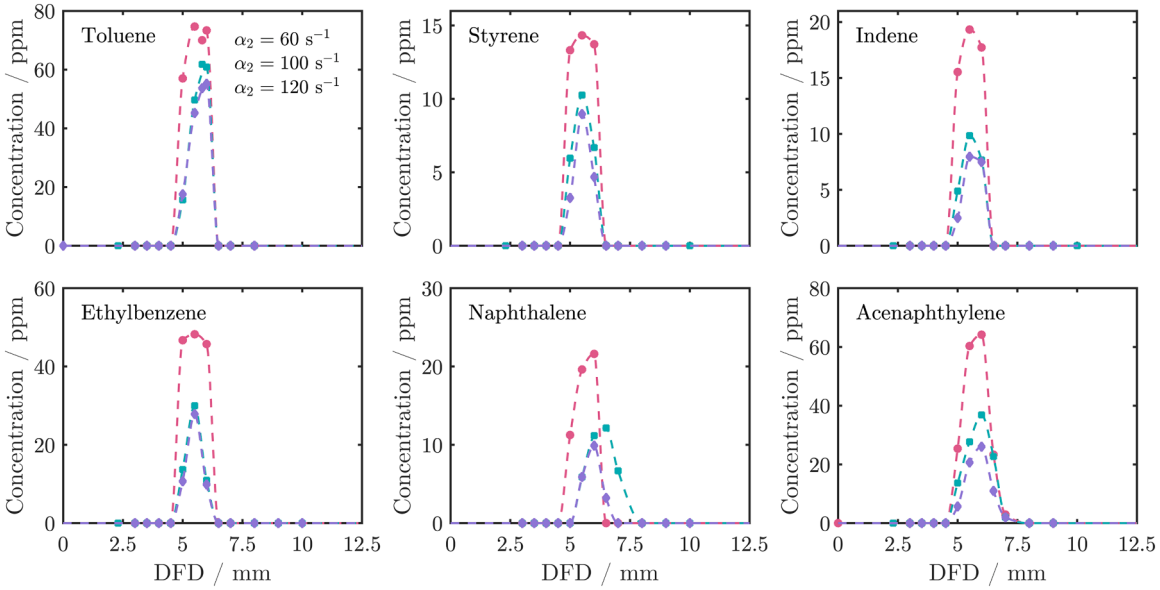

Fig 10. Symbols show the measured volume concentration profiles of A1-based aromatics and PAHs obtained from iso-octane CDFs at a constant fuel mass fraction of 0.60 and varying strain rates of 60 s^{-1}, 100 s^{-1} and 120 s^{-1} as a function of DFD. While the volume concentrations of fluorene, anthracene, and phenanthrene remain below the LOD of the gas-phase diagnostics at a strain rate of 100 s^{-1}, pyrene and higher PAHs were not detected, even at 60 s^{-1}.

the uncertainty of the *CMD* determination. Nevertheless, the overall trends in the evolution of the count median diameter are significant. When the strain rate increases from 60 s^{-1} to 80 s^{-1}, the peak value of *CMD* decreases from about 27 nm to 12 nm for $\sigma_g = 1.4 = const.$ and from approx. 29 nm to 8 nm when assuming variable σ_g according to [47], which may explain the pronounced reduction in soot volume fraction. Similar to variations in fuel mass fraction, particle growth proceeds from the reaction zone towards the stagnation plane, with a profile shape comparable to that of the soot volume fraction.

The molecular structure of the formed soot particles also changes with varying strain rates. As the concentration of large-sized PAHs decreases with increasing strain rate, the size of BSUs embedded within primary particles, i.e., particle maturity, is reduced. This is demonstrated by the decreasing values of $E(m, \lambda_{NIR})$, see Fig 11 and the discussion in Sections 2.4.1 and/or 3.2. The range of detected $E(m, \lambda_{NIR})$ values align with data reported in the literature, covering maturity levels from nascent to mature particles, e.g., [52,53].

4. Summary and concluding remarks

Iso-octane is widely recognized as an important surrogate component for fuels used in internal combustion and aircraft engines. However, experimental studies on soot formation under well-controlled conditions are limited. This work presents a systematic investigation of soot formation in laminar iso-octane counterflow diffusion flames, covering gas-phase composition and soot particle characteristics at varying strain rates and fuel mass fractions. Spatially resolved measurements of temperature, major species, C_1 to C_3 hydrocarbons, PAHs up to three rings, soot volume fraction, particle size, and optical properties were obtained using a combination of intrusive and non-intrusive diagnostics.

Key findings of this study highlight the influence of fuel mass fraction and strain rate on soot formation in iso-octane CDFs. With increasing fuel mass fraction and decreasing strain rate, the concentrations of soot precursor molecules rise, leading to higher soot volume fractions, larger particle sizes, and increased $E(m,\lambda_{NIR})$. Since the molecular fine structure of soot, including BSU length and the carbon-to-hydrogen ratio, is likely linked to the evolution of the refractive-index function for absorption in the near-infrared spectral region $E(m, \lambda_{NIR})$ [50], higher values can be interpreted as indicative of enhanced particle maturity, extended BSUs, and a decreasing carbon-to-hydrogen ratio. Fig. 12 further supports these trends by correlating the maximum soot volume fraction with the maximum naphthalene, A2, concentration and peak $E(m, \lambda_{NIR})$. Gleason et al. [68] demonstrated for CDFs of ethylene that increasing peak temperatures leads to increased soot volume fractions and soot maturity. A similar behavior emerges when combining our datasets on fuel mass fraction and strain rate: higher PAH concentrations are associated with increased soot volume fractions and $E(m, \lambda_{NIR})$, as well as slightly increased peak temperatures. These coupled trends underline the link between precursor concentrations, soot volume fraction, and soot maturity, i.e., the nanostructural features of the formed particles.

By providing insights into soot formation under various boundary conditions of iso-octane CDFs, it serves as a basis for extending the investigations to gasoline, diesel, and both fossil and sustainable aviation fuel surrogates. Additionally, by bridging the gap between gas-phase chemistry and particle formation, this work provides critical data to support the validation and development of detailed kinetic mechanisms and soot models.

Novelty and significance statement

To our knowledge, this is the first study to comprehensively investigate soot formation in laminar iso-octane counterflow diffusion flames (CDFs), spanning gas-phase chemistry to soot particle properties under varying strain rates and fuel mass fractions. The dataset combines spatially resolved measurements of gas-phase species, including minor

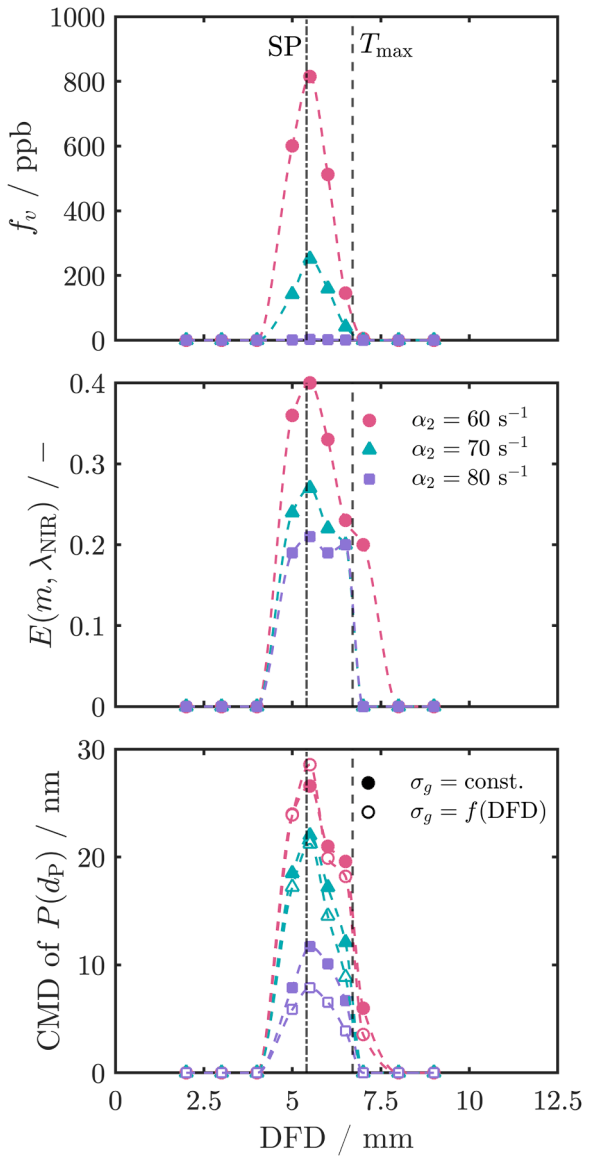

Fig 11. Soot volume fraction, refractive-index function for absorption at the laser excitation wavelength and count median diameter of the primary particle size distribution from iso-octane CDFs at a constant fuel mass fraction of 0.60 and varying strain rates of 60 s^{-1}, 100 s^{-1} and 120 s^{-1} as a function of DFD. The maximum temperature T_{max}, marking the reaction zone, and the stagnation plane, SP, are indicated. Measurement uncertainties and the assumptions on σ_g with open symbols for constant values and closed symbols for variable values are described in detail in the caption of Fig 8.

and major species, C_1 to C_3 hydrocarbons, and PAHs up to three fused aromatic rings, alongside soot volume fractions, particle sizes, and optical properties. Such detailed data in highly controllable iso-octane flames are crucial for elucidating the role of alkane branching in the transition from precursor molecules to soot particles and for providing input to the validation and development of kinetic mechanisms and soot models. In addition, the quantification of optical properties provides new insights into soot maturity, i.e., its molecular fine structure. Thus, the data support the further development of detailed soot models capable of predicting both nanostructural and optical particle properties.

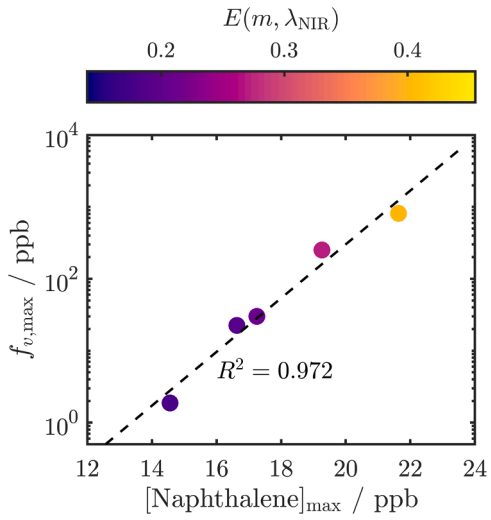

Fig 12. Maximum soot volume fraction as a function of maximum naphthalene, A2, concentration and peak refractive-index function for absorption at the laser excitation wavelength, derived from the dataset. The figure includes a fit of the form $f_{v,max} = 1{\cdot}10^{-5}\exp(0.861\ [A2]_{max})$ with $f_{v,max}$ and the maximum naphthalene concentration $[A2]_{max}$ in ppb, and its coefficient of determination. The peak temperature rises with increasing soot volume fraction from 1807 K, 1826 K, 1850 K, and 1863 K up to 1875 K.

Declaration of generative AI in scientific writing

During the preparation of this work the authors used DeepL and ChatGPT to improve readability. After using these tools, the authors reviewed and edited the content as needed and take full responsibility for the content of the publication.

Data availability

Data will be made available on request.

CRediT authorship contribution statement

Petros Vlavakis: Writing – review & editing, Writing – original draft, Visualization, Methodology, Investigation, Conceptualization. **Fabian P. Hagen:** Writing – review & editing, Writing – original draft, Visualization, Methodology, Investigation, Conceptualization. **Alexandra Loukou:** Writing – review & editing, Supervision, Conceptualization. **Dimosthenis Trimis:** Writing – review & editing, Supervision, Funding acquisition, Conceptualization.

Declaration of competing interest

The authors declare that they have no known competing financial interests or personal relationships that could have appeared to influence the work reported in this paper.

Acknowledgments

This research was funded by the European Union's Horizon 2020 Programme through the ESTiMatE project, grant agreement No. 821418.

Supplementary materials

Supplementary material associated with this article can be found, in the online version, at doi:10.1016/j.combustflame.2025.114513.

References

[1] V. Ramanathan, G. Carmichael, Global and regional climate changes due to black carbon, Nat. Geosci. 1 (2008) 221–227.
[2] C. Chen, O. Dubovik, G.L. Schuster, M. Chin, D.K. Henze, T. Lapyonok, Z. Li, Y. Derimian, Y. Zhang, Multi-angular polarimetric remote sensing to pinpoint global aerosol absorption and direct radiative forcing, Nat. Commun. 13 (2022) 7459.
[3] S.M. Blichner, T. Berntsen, Chapter 6 of the Working Group I Contribution to the IPCC Sixth Assessment Report – Data for Figure 6.12 (v20220815), NERC EDS Centre for Environmental Data Analysis, 2023.
[4] I.M. Kennedy, The health effects of combustion-generated aerosols, Proc. Combust. Inst. 31 (2007) 2757–2770.
[5] R. Niranjan, A.K. Thakur, The Toxicological mechanisms of environmental soot (black carbon) and carbon black: focus on oxidative stress and inflammatory pathways, Front. Immunol. 8 (2017) 1–20.
[6] H.A. Michelsen, M.B. Colket, P.E. Bengtsson, A. D'Anna, P. Desgroux, B.S. Haynes, J.H. Miller, G.J. Nathan, H. Pitsch, H. Wang, A review of terminology used to describe soot formation and evolution under combustion and pyrolytic conditions, ACS Nano 14 (2020) 12470–12490.
[7] J.W. Martin, M. Salamanca, M. Kraft, Soot inception: carbonaceous nanoparticle formation in flames, Prog. Energy Combust. Sci. 88 (2022) 100956.
[8] S.H. Chung, A. Violi, Insights on the nanoparticle formation process in counterflow diffusion flames, Carbon 45 (2007) 2400–2410.
[9] H. Böhm, D. Hesse, H. Jander, B. Lüers, J. Pietscher, H.G. Wagner, M. Weiss, The influence of pressure and temperature on soot formation in premixed flames, Proc. Combust. Inst. 22 (1989) 403–411.
[10] A.E. Karataş, Ö.L. Gülder, Soot formation in high pressure laminar diffusion flames, Prog. Energy Combust. Sci. 38 (2012) 818–845.
[11] Y. Wang, S.H. Chung, Strain rate effect on sooting characteristics in laminar counterflow diffusion flames, Combust. Flame 165 (2016) 433–444.
[12] Y. Wang, S.H. Chung, Soot formation in laminar counterflow flames, Prog. Energy Combust. Sci. 74 (2019) 152–238.
[13] V. Huijnen, A.V. Evlampiev, L.M.T. Somers, R.S.G. Baert, L.P.H. de Goey, The effect of the strain rate on PAH/soot formation in laminar counterflow diffusion flames, Combust. Sci. Technol. 182 (2010) 103–123.
[14] F.P. Hagen, P. Vlavakis, H. Bockhorn, R. Suntz, D. Trimis, From molecular to sub-µm scale: the interplay of precursor concentrations, primary particle size, and carbon nanostructure during soot formation in counter-flow diffusion flames, Combust. Flame 258 (2023) 112729.
[15] R.L. Axelbaum, W.L. Flower, C.K. Law, Dilution and temperature effects of inert addition on soot formation in counterflow diffusion flames, Combust. Sci. Technol. 61 (1988) 51–73.
[16] A. Violi, S. Yan, E.G. Eddings, A.F. Sarofim, S. Granata, T. Favarelli, E. Ranzi, Experimental formulation and kinetic model for JP-8 surrogate mixture, Combust. Sci. Technol. 174 (2002) 399–417.
[17] P. Dagaut, M. Cathonnet, The ignition, oxidation, and combustion of kerosene: a review of experimental and kinetic modeling, Prog. Energy Combust. Sci. 32 (2006) 48–92.
[18] B.C. Choi, S.K. Choi, S.H. Chung, Soot formation characteristics of gasoline surrogate fuels in counterflow diffusion flames, Proc. Combust. Inst. 33 (2011) 609–616.
[19] P. Dagaut, F. Karsenty, G. Dayma, P. Diévart, K. Hadj-Ali, A. Mzé-Ahmed, M. Braun-Unkhoff, J. Herzler, T. Kathrotia, T. Kick, C. Naumann, U. Riedel, L. Thomas, Experimental and detailed kinetic model for the oxidation of a gas to liquid (GtL) jet fuel, Combust. Flame 161 (2014) 835–847.
[20] D.D. Das, C.S. McEnally, T.A. Kwan, J.B. Zimmerman, W.J. Cannella, C.J. Mueller, L.D. Pfefferle, Sooting tendencies of diesel fuels, jet fuels, and their surrogates in diffusion flames, Fuel 197 (2017) 445–458.
[21] X. He, M.T. Donovan, B.T. Zigler, T.R. Palmer, S.M. Walton, M.S. Wooldridge, A. Atreya, An experimental and modeling study of iso-octane ignition delay times under homogeneous charge compression ignition conditions, Combust. Flame 142 (2005) 266–275.
[22] D.F. Davidson, B.M. Gauthier, R.K. Hanson, Shock tube ignition measurements of iso-octane/air and toluene/air at high pressures, Proc. Combust. Inst. 30 (2005) 1175–1182.
[23] Ö.L. Gülder, Burning velocities of ethanol-isooctane blends, Combust. Flame 56 (1984) 261–268.
[24] S.G. Davis, C.K. Law, Laminar flame speeds and oxidation kinetics of iso-octane-air and n-heptane-air flames, Proc. Combust. Inst. 27 (1998) 521–527.
[25] M. Zeng, J. Wullenkord, I. Graf, K. Kohse-Höinghaus, Influence of dimethyl ether and diethyl ether addition on the flame structure and pollutant formation in premixed iso-octane flames, Combust. Flame 184 (2017) 41–54.
[26] I. Frenzel, H. Krause, D. Trimis, Study on the influence of ethanol and butanol addition on soot formation in iso-octane flames, Energy Procedia 120 (2017) 721–728.
[27] F. Liu, Y. Hua, H. Wu, C. Lee, Effect of toluene addition on the PAH formation in laminar coflow diffusion flames of n-heptane and isooctane, Energy & Fuels 32 (2018) 7142–7152.
[28] S. Kruse, A. Wick, P. Medwell, A. Attili, J. Beeckmann, H. Pitsch, Experimental and numerical study of soot formation in counterflow diffusion flames of gasoline surrogate components, Combust. Flame 210 (2019) 159–171.
[29] S.M. Sarathy, U. Niemann, C. Yeung, R. Gehmlich, C.K. Westbrook, M. Plomer, Z. Luo, M. Mehl, W.J. Pitz, K. Seshadri, M.J. Thomson, T. Lu, A counterflow diffusion flame study of branched octane isomers, Proc. Combust. Inst. 34 (2013) 1015–1023.
[30] X. Zhao, L. Xu, C. Chen, M. Chen, Y. Ying, D. Liu, Experimental and numerical study on sooting transition process in iso-octane counterflow diffusion flames: Diagnostics and combustion chemistry, J. Energy Inst. 98 (2021) 282–293.
[31] K.T. Kang, J.Y. Hwang, S.H. Chung, W. Lee, Soot zone structure and sooting limit in diffusion flames: comparison of counterflow and co-flow flames, Combust. Flame 109 (1997) 266–281.
[32] U. Niemann, K. Seshadri, F.A. Williams, Accuracies of laminar counterflow flame experiments, Combust. Flame 162 (2015) 1540–1549.
[33] A.M. Valencia-López, F. Bustamante, A. Loukou, B. Stelzner, D. Trimis, M. Frenklach, N.A. Slavinskaya, Effect of benzene doping on soot precursors formation in non-premixed flames of producer gas (PG), Combust. Flame 207 (2019) 265–280.
[34] R. Khare, P. Vlavakis, T. Von Langenthal, A. Loukou, M. Khosravi, U. Kramer, D. Trimis, Experimental investigation of the effect of hydrogen addition on the sooting limit and structure of methane/air laminar counterflow diffusion flames, Fuel 324 (2022) 124506.
[35] K. Seshadri, F. Williams, Laminar flow between parallel plates with injection of a reactant at high Reynolds number, Int. J. Heat Mass Transfer 21 (1978) 251–253.
[36] P.H. Joo, Y. Wang, A. Raj, S.H. Chung, Sooting limit in counterflow diffusion flames of ethylene/propane fuels and implication to threshold soot index, Proc. Combust. Inst. 34 (2013) 1803–1809.
[37] A. Kalbhor, R. Schmitz, A. Ramirez, P. Vlavakis, F.P. Hagen, F. Ferraro, M. Braun-Unkhoff, T. Kathrotia, U. Riedel, D. Trimis, J. van Oijen, C. Hasse, D. Mira, Experimental and numerical investigation on soot formation and evolution of particle size distribution in laminar counterflow ethylene flames, Combust. Flame 260 (2024) 113220.
[38] C.R. Shaddix, Correcting thermocouple measurements for radiation loss: a critical review, in: Proceedings of the 33rd National & 3rd International Conference, 1999.
[39] F. Carbone, A. Gomez, The structure of toluene-doped counterflow gaseous diffusion flames, Combust. Flame 159 (2012) 3040–3055.
[40] M.M. Sentko, S. Schulz, B. Stelzner, C. Anderlohr, M. Vicari, D. Trimis, Experimental investigation of the pressure influence on flame structure of fuel-rich oxy-fuel methane flames for synthesis gas production, Fuel 286 (2021) 119377.
[41] C. Schulz, B.F. Kock, M. Hofmann, H. Michelsen, S. Will, B. Bougie, R. Suntz, G. Smallwood, Laser-induced incandescence: recent trends and current questions, Appl. Phys. B 83 (2006) 333–354.
[42] H.A. Michelsen, C. Schulz, G.J. Smallwood, S. Will, Laser-induced incandescence: particulate diagnostics for combustion, atmospheric, and industrial applications, Prog. Energy Combust. Sci. 51 (2015) 2–48.
[43] M. Charwath, R. Suntz, H. Bockhorn, Constraints of two-colour TiRe-LII at elevated pressures, Appl. Phys. B 104 (2011) 427–438.
[44] F.P. Hagen, D. Kretzler, T. Häber, H. Bockhorn, R. Suntz, D. Trimis, Carbon nanostructure and reactivity of soot particles from non-intrusive methods based on UV-VIS spectroscopy and time-resolved laser-induced incandescence, Carbon 182 (2021) 634–654.
[45] F. Liu, B.J. Stagg, D.R. Snelling, G.J. Smallwood, Effects of primary soot particle size distribution on the temperature of soot particles heated by a nanosecond pulsed laser in an atmospheric laminar diffusion flame, Int. J. Heat Mass. Trans. 49 (2006) 777–788.
[46] H. Bladh, J. Johnsson, N.-E. Olofsson, A. Bohlin, P.-E. Bengtsson, Optical soot characterization using two-color laser-induced incandescence (2C-LII) in the soot growth region of a premixed flat flame, Proc. Combust. Inst. 33 (2011) 641–648.
[47] F.P. Hagen, P. Vlavakis, M. Seitz, T. Klövekorn, H. Bockhorn, R. Suntz, D. Trimis, Soot nanoparticle sizing in counterflow flames using in-situ particle sampling and differential mobility analysis verified with two-colour time-resolved laser-induced incandescence, Proc. Combust. Inst. 39 (2023) 1119–1128.
[48] H.A. Michelsen, P.E. Schrader, F. Goulay, Wavelength and temperature dependences of the absorption and scattering cross sections of soot, Carbon 48 (2010) 2175–2191.
[49] F.P. Hagen, R. Suntz, H. Bockhorn, D. Trimis, Dual-pulse laser-induced incandescence to quantify carbon nanostructure and related soot particle properties in transient flows – concept and exploratory study, Combust. Flame 243 (2022) 112020.
[50] F.P. Hagen, D. Kretzler, S. Koch, H. Bockhorn, R. Suntz, D. Trimis, H. Kubach, A. Velji, T. Koch, On-line monitoring of carbon nanostructure and soot reactivity in engine exhaust by dual-pulse laser-induced incandescence, Combust. Flame 254 (2023) 112850.
[51] N.-E. Olofsson, J. Simonsson, S. Török, H. Bladh, P.-E. Bengtsson, Evolution of properties for aging soot in premixed flat flames studied by laser-induced incandescence and elastic light scattering, Appl. Phys. B 119 (2015) 669–683.
[52] A.V. Eremin, E.V. Gurentsov, R.N. Kolotushkin, The change of soot refractive index function along the height of premixed ethylene/air flame and its correlation with soot structure, Appl. Phys. B 126 (2020) 125.
[53] P. Desgroux, N. Lamoureux, A. Faccinetto, Combining performances of E(m)-corrected LII and absorption for in situ measurements of the volume fraction of 2-4 nm soot particles, J. Aerosol Sci. 179 (2024) 106385.
[54] F.J. Bauer, K.J. Daun, F.J.T. Huber, S. Will, Can soot primary particle size distributions be determined using laser-induced incandescence? Appl. Phys. B 125 (2019) 109.

[55] S. De Iuliis, F. Migliorini, F. Cignoli, G. Zizak, Peak soot temperature in laser-induced incandescence measurements, Appl. Phys. B 83 (2006) 397–402.
[56] S. Török, M. Mannazhi, P.-E. Bengtsson, Laser-induced incandescence (2λ and 2C) for estimating absorption efficiency of differently matured soot, Appl. Phys. B 127 (2021) 96.
[57] F. Liu, M. Yang, F.A. Hill, D.R. Snelling, G.J. Smallwood, Influence of polydisperse distributions of both primary particle and aggregate size on soot temperature in low-fluence LII, Appl. Phys. B 83 (2006) 383.
[58] D.R. Snelling, F. Liu, G.J. Smallwood, Ö.L. Gülder, Determination of the soot absorption function and thermal accommodation coefficient using low-fluence LII in a laminar coflow ethylene diffusion flame, Combust. Flame 136 (2004) 180–190.
[59] B.F. Kock, B. Tribalet, C. Schulz, P. Roth, Two-color time-resolved LII applied to soot particle sizing in the cylinder of a Diesel engine, Combust. Flame 147 (2006) 79–92.
[60] M. Hofmann, B.F. Kock, T. Dreier, H. Jander, C. Schulz, Laser-induced incandescence for soot-particle sizing at elevated pressure, Appl. Phys. B 90 (2008) 629–639.
[61] H.A. Michelsen, F. Liu, B.F. Kock, H. Bladh, A. Boiarciuc, M. Charwath, T. Dreier, R. Hadef, M. Hofmann, J. Reimann, S. Will, P.-E. Bengtsson, H. Bockhorn, F. Foucher, K.-P. Geigle, C. Mounaïm-Rousselle, C. Schulz, R. Stirn, B. Tribalet, R. Suntz, Modeling laser-induced incandescence of soot: a summary and comparison of LII models, Appl. Phys. B 87 (2007) 503–521.
[62] T. Lehre, H. Bockhorn, B. Jungfleisch, R. Suntz, Development of a measuring technique for simultaneous in situ detection of nanoscaled particle size distributions and gas temperatures, Chemosphere 51 (2003) 1055–1061.
[63] H.A. Michelsen, Understanding and predicting the temporal response of laser-induced incandescence from carbonaceous particles, J. Chem. Phys. 118 (2003) 7012–7045.
[64] H.R. Leider, O.H. Krikorian, D.A. Young, Thermodynamic properties of carbon up to the critical point, Carbon 11 (1973) 555–563.
[65] R. Hadef, K.P. Geigle, W. Meier, M. Aigner, Soot characterization with laser-induced incandescence applied to a laminar premixed ethylene–air flame, Int. J. Therm. Sci. 49 (2010) 1457–1467.
[66] D.R. Snelling, G.J. Smallwood, F. Liu, Ö.L. Gülder, W.D. Bachalo, A calibration-independent laser-induced incandescence technique for soot measurement by detecting absolute light intensity, Appl. Opt. 44 (2005) 6773–6785.
[67] E. Therssen, Y. Bouvier, C. Schoemaecker-Moreau, X. Mercier, P. Desgroux, M. Ziskind, C. Focsa, Determination of the ratio of soot refractive index function E (m) at the two wavelengths 532 and 1064 nm by laser induced incandescence, Appl. Phys. B 89 (2007) 417–427.
[68] K. Gleason, F. Carbone, A. Gomez, Effect of temperature on soot inception in highly controlled counterflow ethylene diffusion flames, Combust. Flame 192 (2018) 283–294.
[69] M. Frenklach, Reaction mechanism of soot formation in flames, Phys. Chem. Chem. Phys. 4 (2002) 2028–2037.
[70] K. Gleason, A. Gomez, Detailed study of the formation of soot precursors and soot in highly controlled ethylene(/toluene) counterflow diffusion flames, J. Phys. Chem. A 127 (2023) 276–285.
[71] N. Olten, S.M. Senkan, On-line measurements of the polycyclic aromatic hydrocarbons (PAH) in counter-flow ethylene diffusion flame, Combust. Sci. Technol. 159 (2000) 1–15.
[72] J. Appel, H. Bockhorn, M. Frenklach, Kinetic modeling of soot formation with detailed chemistry and physics: laminar premixed flames of C_2 hydrocarbons, Combust. Flame 121 (2000) 122–136.
[73] B.G. Sarnacki, H.K. Chelliah, Sooting limits of non-premixed counterflow ethylene/oxygen/inert flames using LII: Effects of flow strain rate and pressure (up to 30 atm), Combust. Flame 195 (2018) 267–281.
[74] C. Betrancourt, X. Mercier, F. Liu, P. Desgroux, Quantitative measurement of volume fraction profiles of soot of different maturities in premixed flames by extinction-calibrated laser-induced incandescence, Appl. Phys. B 125 (2019) 16.
[75] K.O. Johansson, F. El Gabaly, P.E. Schrader, M.F. Campbell, H.A. Michelsen, Evolution of maturity levels of the particle surface and bulk during soot growth and oxidation in a flame, Aerosol Sci. Technol. 51 (2017) 1333–1344.
[76] C.J. Sung, J.B. Liu, C.K. Law, Structural response of counterflow diffusion flames to strain rate variations, Combust. Flame 102 (1995) 481–492.